Chemical Engineering Science 284 (2024) 119414

Contents lists available at ScienceDirect

Chemical Engineering Science

journal homepage: www.elsevier.com/locate/ces

Investigating the effect of sintering rate and solvent type on the liquid transport kinetics of α-alumina powder compacts

Mohammed Al-Sharabi [a], Daniel Markl [b,c], Vincenzino Vivacqua [d], Prince Bawuah [a], Natalie MacLean [b,c], Andrew P.E. York [e], J. Axel Zeitler [a,*]

[a] Department of Chemical Engineering and Biotechnology, University of Cambridge, Cambridge CB3 0AS, UK
[b] Strathclyde Institute of Pharmacy and Biomedical Sciences, University of Strathclyde, 161 Cathedral Street, Glasgow G4 0RE, UK
[c] Centre for Continuous Manufacturing and Advanced Crystallisation (CMAC), University of Strathclyde, 99 George Street, Glasgow G1 1RD, UK
[d] Johnson Matthey Technology Centre, P.O. Box 1, Belasis Avenue, Billingham TS23 1LB, UK
[e] Johnson Matthey Technology Centre, Blounts Court, Sonning Common, Reading RG4 9NH, UK

ARTICLE INFO

Keywords:
Porous catalysts
α-alumina
Terahertz pulsed imaging
Liquid transport
Sintering
Solvents

ABSTRACT

The ceramic materials' properties and the penetrating liquid both influence liquid transport into ceramic catalytic materials. Terahertz pulsed imaging (TPI) in combination with a flow cell was used to investigate the transport process of polar and less polar solvents into a range of α-alumina powder compacts. The TPI results show that the alumina samples with the largest heating rate (200 °C h^{-1}) have the fastest water transport. The TPI results also reveal that 1-octanol takes much longer to transport through the alumina samples than water, as the viscosity of 1-octanol is much larger than that of water. Since 1-octanol is semi-transparent to terahertz radiation, it was possible to study the liquid transport process and the structural changes behind the liquid front, such as the change in the refractive index of the compact and the fill fraction of 1-octanol in the compact as a function of time.

1. Introduction

Porous ceramics have been extensively used in several industrial applications, such as thermal insulators (Wu et al., 2018), membranes for filtration (Werner et al., 2014; Nagasawa et al., 2020), substrates for electrodes in fuel cells (Amaya et al., 2017) and catalyst supports (Faure et al., 2011; Pechenkin et al., 2015). The performance of such materials depends on their pore structure properties, such as porosity, pore size, shape, orientation, distribution and connectivity, as well as surface area (Hammel et al., 2014; Wan et al., 2020). Ceramic powders are generally compacted by uniaxial die pressing in a rigid die, i.e. uniaxial die compaction, to produce a porous powder compact (Chen et al., 2007; Montilha et al., 2018). In addition, various additives are added to ceramic powders to achieve the desired flowability and cohesion of particles (Kumar et al., 2014).

The compaction of powder is followed by sintering (firing), a typical densification process for acquiring the desired density and strength of the compacts through the heat treatment of green bodies at high temperatures (Kempen et al., 2019). The inhomogeneous density distribution in the powder compact often results in heterogeneous microscopic and macroscopic shrinkage of the compact, which can potentially cause some defects in the sintered product (Okuma et al., 2018). The powder properties and manufacturing parameters, such as compaction pressures, heating rates of sintering, sintering time and temperature, affect the sintering process (Boccaccini and Trusty, 1998). Furthermore, the sintering process impacts the pore structure properties of the final compact as sintering results in the shrinkage of the pores through the rearrangement of particles, relative sliding of particles or diffusion (Kim et al., 2021). The microstructure characteristics of the compact affect its wettability and hence the liquid transport through the compact (Al-Sharabi et al., 2021). Given that the microstructure of the compact changes during the sintering of the green body, it is crucial to investigate the impact of the sintering parameters, such as the heating rate, on the pore structure properties, and hence the liquid transport process to enhance the design and performance of catalytic materials in the form of ceramic powder compacts.

Aluminium oxide (Al_2O_3), also commonly known as alumina, is one of the most widely used ceramic materials due to its low cost and the retention of strength and stability at high temperatures (Munro, 1997; Yang et al., 2020). α-Alumina is a stable alumina phase with desirable

* Corresponding author.
E-mail address: jaz22@cam.ac.uk (J.A. Zeitler).

https://doi.org/10.1016/j.ces.2023.119414
Received 8 June 2023; Received in revised form 30 September 2023; Accepted 18 October 2023
Available online 23 October 2023

features, such as high strength and hardness, high temperature and corrosion resistance (Luo et al., 2018). This alumina phase has been widely used in many industrial applications, such as adsorbants (Choi et al., 2020) and catalytic supports (Rytter et al., 2019).

Liquid transport into porous catalytic materials is an important phenomenon encountered in a large number of applications, such as water transport into the porous cathode catalytic layer of fuel cell (Das et al., 2010), the migration of solvent into or out of the pores of the catalyst support during the synthesis processes of porous supported catalysts, such as impregnation and drying (Munnik et al., 2015; Nijhuis et al., 2001), as well as the mass transport during the heterogenous catalysis over porous catalysts (Sievers et al., 2016; Rytter et al., 2019). Since different solvents are used during the manufacturing of catalytic materials for the deposition of the different active catalysts on the catalyst support as well as during the liquid-phase reactions over solid heterogenous catalysts, it is crucial to investigate the mass transport of various solvents into porous catalytic materials to understand better the impact of the type of solvent on their transport process in porous catalytic materials.

Several studies have investigated the mass transport characteristics of various porous heterogeneous catalysts using many different techniques. Jaine and Mucalo (2015) used the Washburn capillary rise technique to determine the wetting rates and contact angles of several different organic solvents in various catalyst support materials. Zhokh and Strizhak (2017) utilised gas chromatography to study the methanol transport through a range of zeolite/alumina catalysts composed of different zeolite/alumina ratios. Mantle et al. (2010) applied the pulsed-field gradient (PFG)-NMR technique to study the effective self-diffusivity of alcohols within supported catalysts consisting of gold supported on titania, silica and ceria as well as gold-palladium alloy nanoparticles supported on titania. D'Agostino et al. (2012) also used PFG-NMR to measure the self-diffusion coefficients of various organic liquids within mesoporous catalyst supports used in heterogeneous catalysis, i.e. titania, alumina and silica. Lysova et al. (2005) performed MRI measurements to study the transport of an aqueous solution of H_3PO_4 into alumina pellets during impregnation and investigate the distribution of the adsorbed phosphate within the dried support. Lysova et al. (2010) also used the MRI technique to study the transport of an aqueous solution of $(NH_4)_6Mo_7O_{24}$ into an alumina pellet and investigate the distribution of Mo in the solid phase within the dried alumina support.

Terahertz pulsed imaging (TPI) is another promising technique for investigating the liquid transport kinetics of ceramic catalytic materials due to the transparency of most ceramic materials to terahertz radiation (Jonuscheit, 2018; Al-Sharabi et al., 2021). TPI has recently been applied in several studies in the pharmaceutical field to resolve the liquid transport and swelling kinetics in a wide range of simple and complex pharmaceutical tablets with different structural characteristics to better understand the disintegration process of such porous compacts upon contact with water (Yassin et al., 2015a,b; Markl et al., 2017, 2018; Al-Sharabi et al., 2020; Skelbæk-Pedersen et al., 2020; Dong et al., 2021; Dong and Zeitler, 2022; Dong et al., 2023; Soundaranathan et al., 2023). Upon the success of using TPI for the investigation of water transport into rigid ceramic powder compacts made from functionalised calcium carbonate powder that can be used as a pharmaceutical filler for highly porous tablets (Markl et al., 2018), Al-Sharabi et al. (2021) further developed and used the TPI method to investigate the water transport kinetics of a range of α-alumina powder compacts that were manufactured at different compaction and heat treatment conditions. The solvent used in all the previously mentioned TPI studies was water. In addition to resolving the water transport kinetics, Obradovic et al. (2007) used the terahertz method to quantify the penetration of acetone into a range of swelling polymeric materials.

This work aimed at using the TPI method to understand better the impact of the heating rate of sintering on the water ingress kinetics of a range of α-alumina powder compacts prepared at different compaction forces and sintered at 1200 °C with three different heating rates (100 °C h^{-1}, 150 °C h^{-1} and 200 °C h^{-1}). In addition, this work aimed at applying the TPI technique to study the 1-octanol transport into a range of α-alumina powder compacts prepared at different compaction forces and heat treatment conditions, i.e. unfired and fired at 1200 °C with a heating rate of 200 °C h^{-1}.

2. Materials and methods

2.1. Sample preparation

2.1.1. Materials and compaction

The raw powder mixture and compaction process followed the procedure reported in (Al-Sharabi et al., 2021). A powder mixture consisting of mainly α-alumina with a maximum of 5% m/m of polymeric organic additives and 1% m/m of inorganic additives (Granalox® NM 99, Nabaltec AG, Schwandorf, Germany) was used to prepare flat-faced cylindrical pellets via direct compaction. The compaction process was conducted using a compaction simulator (Styl'One Evolution, Medelpharm, Beynost, France) by varying the filling weight of the feed powder while keeping the thickness and diameter of the sample fixed to obtain different porosities of the pellet. Four sets of pellets with various porosities were produced using compaction forces of 7 kN, 23 kN, 40 kN and 58 kN. The resulting pellets have a thickness and diameter of around 2 mm and 11.28 mm, respectively, and will be referred to as unfired samples.

2.1.2. Sintering

Sintering was performed on three additional sets of compacted samples using the same compaction conditions and procedure used for the unfired samples. The three sets were fired at the same temperature (1200 °C) and dwell time (6 h) but at three different ramp (heating) rates (100 °C h^{-1}, 150 °C h^{-1} and 200 °C h^{-1}). The firing process was then followed by cooling the samples to room temperature at around 100 °C h^{-1}.

2.2. Determination of porosity

The nominal porosity, $f_{\text{nominal}}(\%)$, of the unfired and fired samples was determined using Equation (1) with ρ_{true}, D, H and W as the true density, diameter, thickness and weight, respectively (Al-Sharabi et al., 2020). The true density of the alumina powder was measured using helium pycnometry (Micromeritics ACCUPYC 1340, Austin (TX), USA) and reported in our previous study (Al-Sharabi et al., 2021). A summary of the 16 batches used for the liquid transport measurements with their corresponding $f_{\text{nominal}}(\%)$ is provided in Table 1.

$$f_{\text{nominal}}(\%) = \left(1 - \frac{4W}{\pi D^2 H \rho_{\text{true}}}\right) \times 100 \tag{1}$$

Table 1
The nominal porosity, $f_{\text{nominal}}(\%)$, of the samples determined by Equation (1). The samples were fired at 1200 °C with heating rates of (100 °C h^{-1}, 150 °C h^{-1} and 200 °C h^{-1}). 10 samples per batch were used to calculate the average $f_{\text{nominal}}(\%)$ and its standard deviation.

Compaction force (kN)	7	23	40	58
Unfired	39.18 ± 0.12	36.09 ± 0.17	34.57 ± 0.06	33.46 ± 0.10
Fired at 100 °C h^{-1}	36.39 ± 0.15	32.51 ± 0.15	31.07 ± 0.12	29.94 ± 0.15
Fired at 150 °C h^{-1}	36.17 ± 0.17	32.54 ± 0.09	31.15 ± 0.13	30.20 ± 0.19
Fired at 200 °C h^{-1}	36.12 ± 0.22	33.00 ± 0.18	31.44 ± 0.19	30.29 ± 0.13

2.3. Terahertz time-domain spectroscopy

Terahertz time-domain spectroscopy (THz-TDS) measurements were conducted to measure the effective refractive index, n_{eff}, of the alumina samples using a commercial terahertz system (TeraPulse 4000, Teraview Ltd., Cambridge, UK) operating in a transmission configuration. The THz-TDS measurements were performed for ten samples per batch. These measurements were conducted by comparing the measured terahertz waveforms of the sample and a reference, i.e. an empty spectrometer with no sample in the compartment. Dry nitrogen gas was purged into the sample compartment during the measurements to reduce the effect of the absorption of the terahertz signal by the water vapour (Al-Sharabi et al., 2020). Each transmission measurement lasted for 40 s, with 20 waveforms being co-averaged to enhance the signal-to-noise ratio. The acquired time-domain terahertz signals of the reference and the sample were transformed to the frequency-domain via fast Fourier transform (FFT) to determine the frequency-dependent effective refractive index, $n_{\text{eff,FD}}$, using (Bawuah et al., 2020)

$$n_{\text{eff,FD}}(\upsilon) = 1 + \frac{c\theta(\upsilon)}{2\pi\upsilon H}, \tag{2}$$

where υ is the frequency, c is the speed of light in vacuum, and θ is the phase difference between the sample waveforms and reference. The $n_{\text{eff,FD}}$ was determined at 1 THz for all the samples considering that $n_{\text{eff,FD}}$ is constant and no absorption peaks were observed at the selected frequency.

The n_{eff} of 1-octanol (99% purity, Alfa Aesar) was also measured using a liquid cell in combination with the THz-TDS system. The terahertz reference waveform was acquired by measuring through two quartz windows placed on top of each other in the liquid cell. For the sample measurement, a spacer with a thickness of 1.15 mm was placed between the two quartz windows in the liquid cell to create space for the sample. The sample, i.e. 1-octanol, was injected into the liquid cell using a pipette and the terahertz sample waveform was acquired by measuring through the quartz windows and 1-octanol. The data was processed to determine the n_{eff} at 1 THz.

2.4. Terahertz pulsed imaging

Terahertz pulsed imaging (TPI) was used to measure the one-dimensional (1D) solvent transport kinetics of the α-alumina powder compacts. The *in situ* TPI measurements were performed using a new bespoke flow cell in combination with the same commercial terahertz system used for the THz-TDS measurements but operating in a reflection configuration. The flow cell was first designed and used by Al-Sharabi et al. (2021) for the in-situ investigation of the water transport kinetics in α-alumina samples prepared over a wide range of compaction forces and sintering conditions. The terahertz system operates with a fibre-based reflection probe mounted on a linear scale to optimise its position before the experiment. The probe had a silicon lens with an 18 mm focal length. In order to monitor the liquid transport process, continuous acquisition of the TPI data was conducted at an acquisition rate of 15 Hz. The acquired terahertz waveforms cover a total time delay of 45 ps. A detailed explanation of the principle, experimental setup and procedure, and TPI data acquisition and processing can be found in our previous study (Al-Sharabi et al., 2021).

Three pellets per batch were used for the TPI liquid transport measurements to obtain each batch's averaged time-resolved penetration profiles. The first set of the TPI measurements was conducted for the in-situ investigation of the penetration of water into α-alumina powder compacts (cold compaction at compaction forces of 7 kN to 58 kN and fired at 1200 °C with three different heating rates of 100 °C h^{-1}, 150 °C h^{-1} and 200 °C h^{-1}). The second set of the TPI measurements was performed to study the transport of 1-octanol into α-alumina powder compacts (cold compaction at compaction forces of 7 kN to 58 kN, unfired and fired at 1200 °C with a heating rate of 200 °C h^{-1}). Examples of the in-situ monitoring of the liquid transport process of water and 1-octanol in the alumina samples using TPI are illustrated in Fig. 1.

2.5. X-ray microcomputed tomography

X-ray microcomputed tomography (XμCT) measurements were conducted on the alumina samples that were compacted at 7 kN, 23 kN, 40 kN and 58 kN and subsequently fired at three different heating rates of 100 °C h^{-1}, 150 °C h^{-1} and 200 °C h^{-1} to 1200 °C to visualise the microstructure of these samples and detect the presence/absence of cracks after firing, which can potentially have an impact on the water penetration kinetics in such samples. The samples were scanned at an isotropic voxel size of 4.44 μm using a Skyscan 1172 instrument (Bruker, Antwerp, Belgium) with a cone-beam configuration with the application of an aluminium copper (Al+Cu) filter. Each alumina sample was fixed on the sample holder using double-sided sticky tape. The 3D scanning of the sample was conducted by rotating the sample through 180 °C and collecting the projection images at a rotation step of 0.25° and an exposure time of 6000 ms. The shadow-projected images were subsequently reconstructed using NRecon software (Bruker, Version: 1.7.4.2) to obtain cross-section images of the scanned sample. These reconstructed images were then aligned and visualised at a specific position of interest using DataViewer (Bruker, Version: 1.5.3.4).

2.6. Contact angle measurements

The dynamic contact angle was measured for three compacts per batch to determine the wettability of the alumina samples by water and 1-octanol and to investigate the effect of the wettability on the liquid transport kinetics of such samples. The dynamic contact angle between the

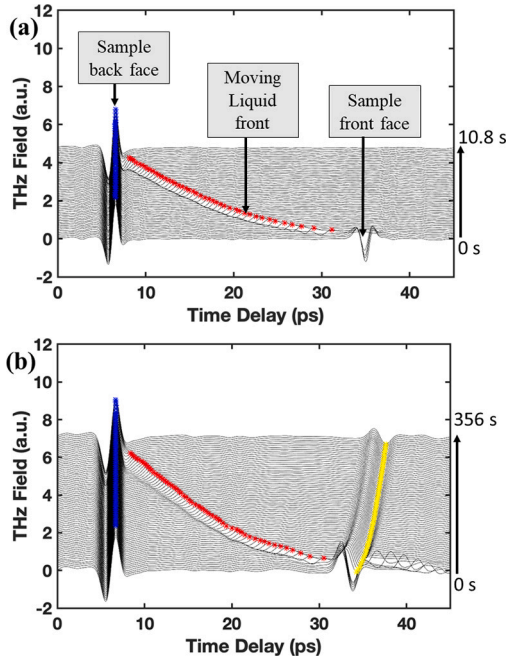

Fig. 1. The deconvolved terahertz waveforms presented in stacked plots to show (a) the water penetration (flagged in red) into an alumina sample compacted at 7 kN and subsequently fired at 1200 °C with a heating rate of 100 °C h^{-1} and (b) the 1-octanol penetration (flagged in red) into an unfired alumina sample compacted at 7 kN. Each third (a) and fifth (b) deconvolved waveform was plotted with an offset of 0.03 a.u. (a) and 0.02 a.u. between each deconvolved waveform for the water and 1-octanol, respectively. Fifteen waveforms were averaged during the 1-octanol TPI transport measurements of the unfired sample due to the slow transport process. The first TPI measurement corresponds to the first waveform at the bottom of the stacked plot. The total duration (in seconds) of the full penetration of the liquid into the sample is represented by the arrow on the right of each plot.

sample surface and a droplet of 1-octanol was measured by drop shape analysis (Krüss DSA30, Krüss GmbH, Hamburg, Germany). For each sample, video recordings were taken at 30 frames per second. The video files were analysed using MATLAB (2019a, Mathworks, Massachusetts, USA) to measure the contact angle for each frame of the recording. The contact angle profiles were then fit with a two-phase exponential decay model (Eq. (3)) using GraphPad Prism 8 (Version: 8.3.1, GraphPad Software LLC, San Diego).

$$\theta_c(t) = \theta_{c,p} + s_f e^{-k_f \cdot t} + s_s e^{-k_s \cdot t} \tag{3}$$

$$s_f = \theta_{c,0} \cdot x_{fs}$$

$$s_s = \theta_{c,0}\left(1 - x_{fs}\right)$$

$\theta_{c,0}$ and $\theta_{c,p}$ are the contact angles at initial and infinite time, respectively. k_f and k_s are the rate constants for the fast and slow phases, respectively. The fraction of time dominated by the fast phase of the reaction is described as x_{fs}.

3. Results and discussion

3.1. Analysis of effective refractive index

The $n_{eff,FD}$ of the alumina powder compacts measured by the THz-TDS technique is presented as a function of the $f_{nominal}$ of these compacts as shown in Fig. 2. A linear relation between $n_{eff,FD}$ and $f_{nominal}$ is observed within each set of heat treatment conditions. $n_{eff,FD}$ is inversely proportional to the porosity of the compact ($f_{nominal}$). Due to the presence of polymer binder in the unfired sample $n_{eff,FD}$ is lower than the fired samples. The polymer binder completely burns during the firing process, which explains the difference in refractive index between the fired and unfired samples. Decreasing the heating rate results in a slight increase in $n_{eff,FD}$ for all compaction forces except the lowest (7 kN). This suggests that the firing process not only results in the removal of the polymeric binder but also causes other structural changes in the compact upon being subjected to different heating rates of firing.

3.2. In situ visualisation of liquid transport

The deconvolved terahertz waveforms acquired from each TPI measurement are presented in a stacked plot for each sample as illustrated in Figs. 3, 4, A.17 and A.18 with an offset between each deconvolved waveform to show the movement of the penetrating solvent in the alumina sample as a function of time. Figs. 3 and A.17 show the stacked plots, i.e. waterfall plots, comparing the water penetration into the alumina samples at different compaction forces within each set of heating rate, i.e. 100 and 150 °C h^{-1}. The waterfall plots of the water penetration into the alumina samples at the different compaction forces at the heating rate of 200 °C h^{-1} have been reported in our previous study (Al-Sharabi et al., 2021). On the other hand, Figs. 4 and A.18 show the 1-octanol penetration into the alumina samples at the different compaction forces within each heat treatment condition, i.e. unfired and fired at 1200 °C with a heating rate of 200 °C h^{-1}.

The relative difference in the refractive indices of the two media through which the terahertz pulse travels determines the magnitude of the amplitude of the terahertz reflection peak (Markl et al., 2018). The sign of the reflection peak amplitude, i.e. positive or negative, shows whether

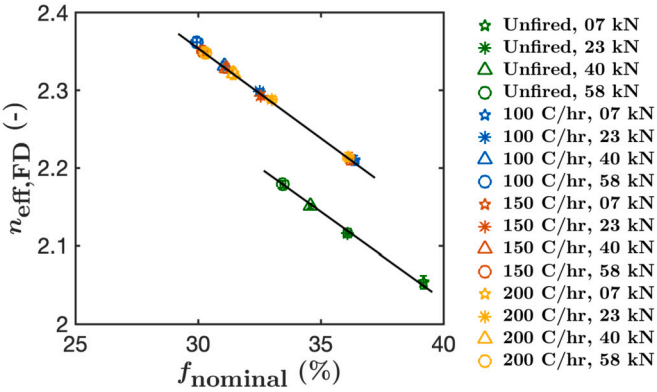

Fig. 2. The frequency-dependent effective refractive index at a frequency of 1 THz, $n_{\text{eff,FD}}$, of the unfired and fired alumina samples at different compaction forces of 7 kN, 23 kN, 40 kN and 58 kN as a function of the nominal porosity, f_{nominal}. The fired samples were fired at different ramp rates of 100 °C h^{-1}, 150 °C h^{-1} and 200 °C h^{-1} to reach the terminal firing temperature of 1200 °C. The black lines are added to guide the eye.

the propagation of the terahertz pulse is into or out of a medium with lower or higher refractive index (Al-Sharabi et al., 2021). A positive reflection peak is observed upon the propagation of the pulse from a medium with a lower refractive index to a medium with a higher refractive index (Al-Sharabi et al., 2020). Therefore, the propagation of the terahertz pulse from air ($n_{\text{air}} = 1$) to the sample (n_{eff} in Fig. 2) and then to air results in positive and negative reflection peaks from the sample back face and front face facing the liquid, respectively, before the liquid comes in contact with the dry sample. The part of the sample wetted with the solvent, i.e. water or 1-octanol ($n_{\text{water}} \approx 2.1$ as reported by Pickwell and Wallace (2006) and $n_{\text{1-octanol}} \approx 1.484$ at 1 THz), has a higher refractive index in comparison with the dry part of the sample, and therefore a positive reflection peak is observed for the penetrating liquid front.

The positive peak, corresponding to the reflection from the back face of the alumina pellet, does not disappear after the complete wetting of the sample with water. This observation confirms that the alumina samples do not disintegrate in water given their rigid and non-soluble nature in this solvent, as previously observed by Al-Sharabi et al. (2021). Similarly, the terahertz results show that the alumina pellets equally do not dissolve or disintegrate in 1-octanol: the back face reflection peak remains detectable even after the 1-octanol completely penetrates the sample. It has been shown in previous studies that the TPI method provides information on the swelling of a porous compact, which is indicated by a shift in the temporal location of the reflection peak from the back face of the sample due to a change in the sample thickness (Obradovic et al., 2007; Yassin et al., 2015b,a; Al-Sharabi et al., 2020). The terahertz results show that the temporal position of the positive peak, corresponding to the reflection from the back face of the alumina pellet, remains unchanged. This indicates that the sample thickness remains constant and no swelling occurs in either water or in 1-octanol.

The terahertz pulse consists of an alternating external electric field, which couples strongly with the molecular dipole in polar molecules but cannot couple effectively with non-polar molecules (Lapuerta et al., 2020). Beyond the dielectric relaxations of the solvent molecules themselves, terahertz radiation is at resonance with energies corresponding to intermolecular interactions, such as hydrogen bonds and London dispersion forces. This can result in additional absorption based on the composition of the material that is interacting with the terahertz radiation. Water is a highly mobile solvent with a strong dipole known to absorb terahertz radiation strongly (Xu et al., 2006; Lewis, 2017); due to the strong absorption it is impossible to observe in reflection what happens in the wetted pellet behind the water front as shown in Fig. 3. In contrast, it is possible to see the reflection peak from the front face of the pellet after coming in contact with 1-octanol (Fig. 4) as octanol is less polar and less mobile due to its increased size, and hence are less absorbing to terahertz radiation (Lapuerta et al., 2020). The position of the reflection peak from the front face of the sample is observed to shift to the right upon the penetration of 1-octanol into the sample. It is important to highlight that this is not the result of any dimensional changes of the samples pellet, i.e. swelling, but due to the change in refractive index of the wetted matrix. As air in the pores of the alumina samples is replaced with 1-octanol the n_{eff} of the wetted material increases resulting in an increase of the time delay of the reflected terahertz pulse. The change in the time delay can be used to calculate the change in n_{eff} of the alumina sample upon the penetration of 1-octanol into the sample.

3.3. Quantification of the liquid transport process

3.3.1. Effect of heating rate of firing on the water transport

Fig. 5 shows the averaged water penetration depth as a function of time for the alumina samples that were compacted at 7, 23, 40 and 58 kN and subsequently fired at 1200 °C with heating rates of 100, 150 and 200 °C h^{-1}. The water penetration profiles show that the alumina pellets with the highest heating rate of 200 °C h^{-1} have the fastest rate of water transport at any given compaction force. A similar rate of water transport is observed for the samples fired at heating rates of 100 and 150 °C h^{-1} within each of the compaction forces of 7, 23 and 40 kN. However, a difference in the rate of water transport is observed between the heating rates of 100 and 150 °C h^{-1} at the compaction force of 58 kN where the samples fired at a heating rate of 100 °C h^{-1} exhibits a faster rate of water ingress.

The XμCT measurements were conducted to investigate the presence of cracks during the firing process at different heating rates, potentially affecting the water penetration rate into the alumina samples at the different compaction forces. The XμCT results presented in Fig. 6 show that all the fired samples, over the range of rates and compaction forces, exhibit a homogenous structure and no cracks are apparent. Therefore, we assume that the transport measurements are not affected by any crack structures in the matrix.

3.3.2. Effect of the type of solvent on the transport process

The averaged liquid penetration profiles showing the transport of 1-octanol into the unfired and fired alumina samples with the different compaction forces are shown in Fig. 7. These profiles reveal that the change in the compaction force, and hence the porosity of the compact, clearly

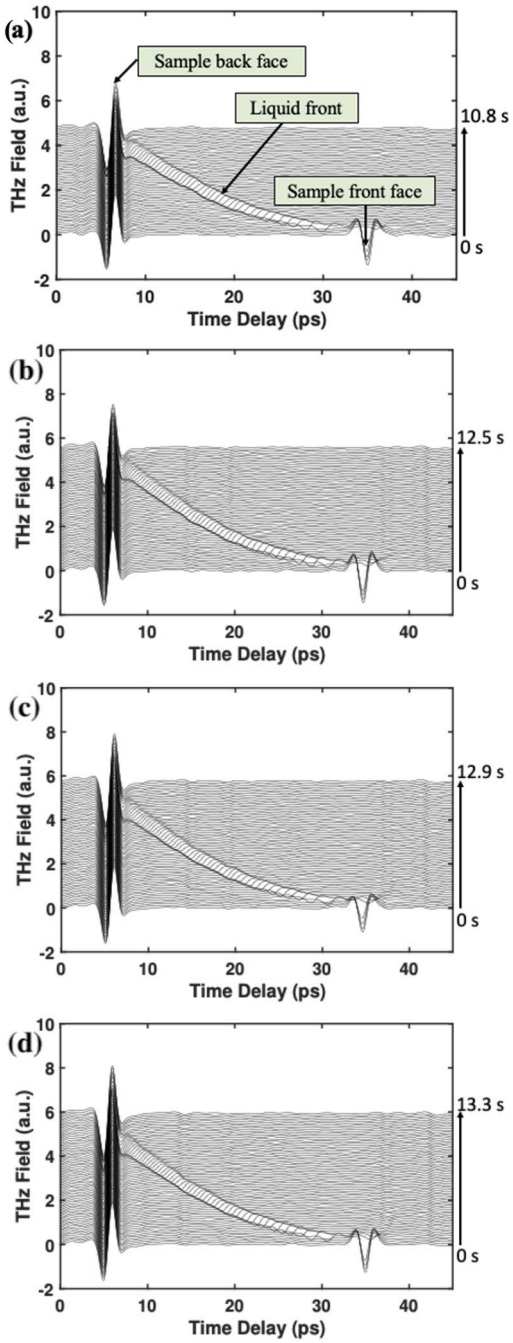

Fig. 3. The deconvolved terahertz waveforms presented in stacked plots (waterfall plots) to show the water penetration into a set of alumina samples that were compacted at (a) 7 kN, (b) 23 kN, (c) 40 kN and (d) 58 kN and subsequently fired at 1200 °C with a heating rate of 100 °C h^{-1}. Each third deconvolved waveform was plotted with an offset of 0.03 a.u. between each deconvolved waveform to enable the visualisation of the water front movement into the alumina sample. The total duration (in seconds) of the full water penetration into the sample is represented by the arrow on the right of each plot.

influences the transport process of 1-octanol in the alumina samples. The 1-octanol propagates faster the more porous the sample is. This behaviour is observed for the unfired and fired samples. Therefore, it is clear from the TPI results that the microstructure characteristics of the sample, i.e. porosity, influence the penetration rate of 1-octanol into the alumina samples.

Fig. 8 shows that the 1-octanol transport is faster in the unfired alumina samples than the fired samples at the same compaction force. The unfired samples exhibit higher porosity than the fired samples at the same compaction force since the firing process results in the shrinkage of the compact and hence a decrease in its porosity. The higher lipophilicity of the unfired samples containing the polymeric additives further explains the faster transport of 1-octanol in such samples compared to the fired samples at the same compaction conditions. In contrast, in our previous work (Al-Sharabi et al., 2021), the TPI results showed that the unfired samples had a slower rate of water transport as such samples have lower wettability due to the polymeric additives. The increase in transport rate observed in the terahertz results of the 1-octanol transport were confirmed by contact angle measurements (Fig. 9), which show that the initial contact angle of the alumina samples fired at 1200 °C have larger values relative to the unfired samples at the same compaction force, except the samples compacted at 40 kN, which is an outlier. The smaller contact angles of the unfired samples confirm that such samples are more wettable and, therefore, have faster transport rates than the fired samples.

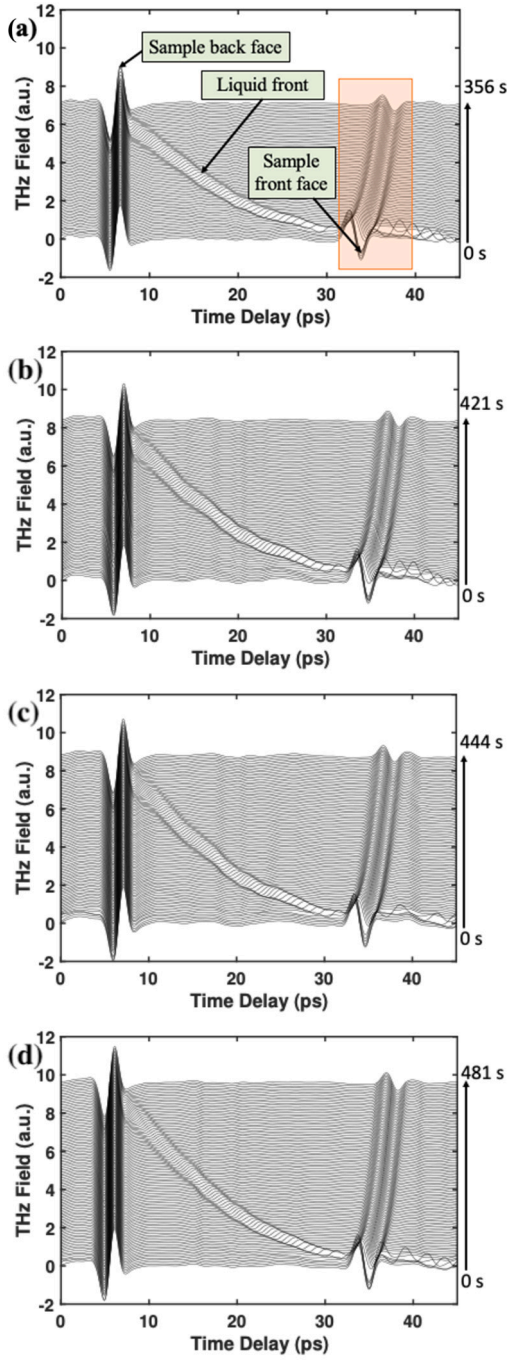

Fig. 4. The deconvolved terahertz waveforms presented in stacked plots to show the 1-octanol penetration into a set of unfired alumina samples that were compacted at (a) 7 kN, (b) 23 kN, (c) 40 kN and (d) 58 kN. Each fifth deconvolved waveform was plotted with an offset of 0.02 a.u. between each deconvolved waveform to enable the visualisation of the 1-octanol front movement into the alumina sample. The total duration (in seconds) of the full penetration of 1-octanol into the sample is represented by the arrow on the right of each plot.

A comparison between the rates of the penetration of water and 1-octanol into the unfired and fired alumina samples at the different compaction forces is also illustrated in the liquid penetration profiles in Fig. 8 and discussed later after fitting the power law (Equation (9)) as shown in Fig. 16. The water penetration rate is higher than the rate of the 1-octanol transport at the same compaction force and heat treatment condition, i.e. unfired and fired, indicating the slower transport process of 1-octanol into the alumina sample. The dynamic viscosities of water and 1-octanol at 20 °C are 1.002 mPa s (Al-Sharabi et al., 2021) and 9.183 mPa s (Trenzado et al., 2003), respectively. Therefore, the slower transport of 1-octanol can be attributed to the fact that 1-octanol has a much larger dynamic viscosity than water, which results in a much slower penetration of the 1-octanol into the porous compact. This is consistent with the definition of the Lucas-Washburn equation for a laminar flow in a porous medium when neglecting the effect of gravity and inertia forces, as expressed in Equation (4), which shows that the penetration rate decreases with an increase in the dynamic viscosity of the liquid penetrating the porous sample (Markl et al., 2018; Cai et al., 2021).

$$L(t) = \sqrt{\frac{R_{h,eq}\gamma \cos\theta t}{2\mu}}, \tag{4}$$

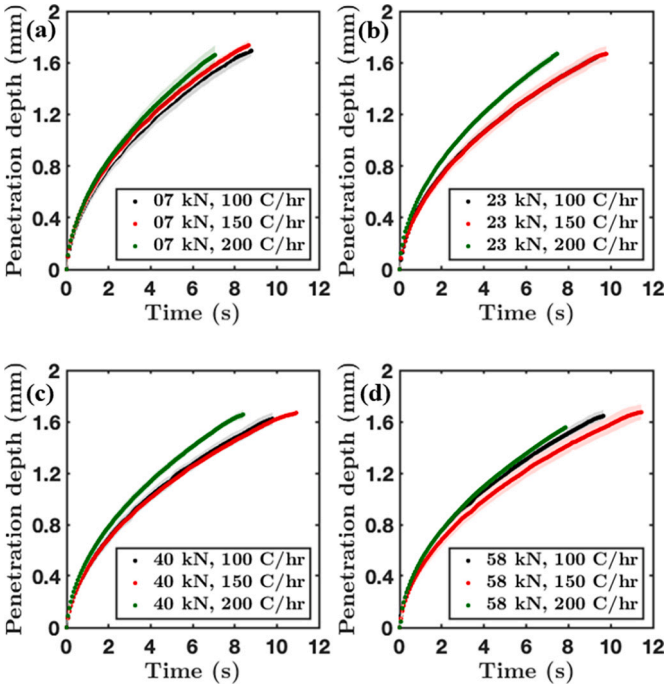

Fig. 5. The water penetration depth as a function of time of the alumina samples compacted at 7, 23, 40 and 58 kN and subsequently fired at 1200 °C with heating rates of 100, 150 and 200 °C h^{-1}. The shaded area of each profile corresponds to the standard deviation of each batch. The data of the water transport into the alumina samples fired at 1200 °C with a heating rate of 200 °C h^{-1} have been reproduced from Al-Sharabi et al. (2021).

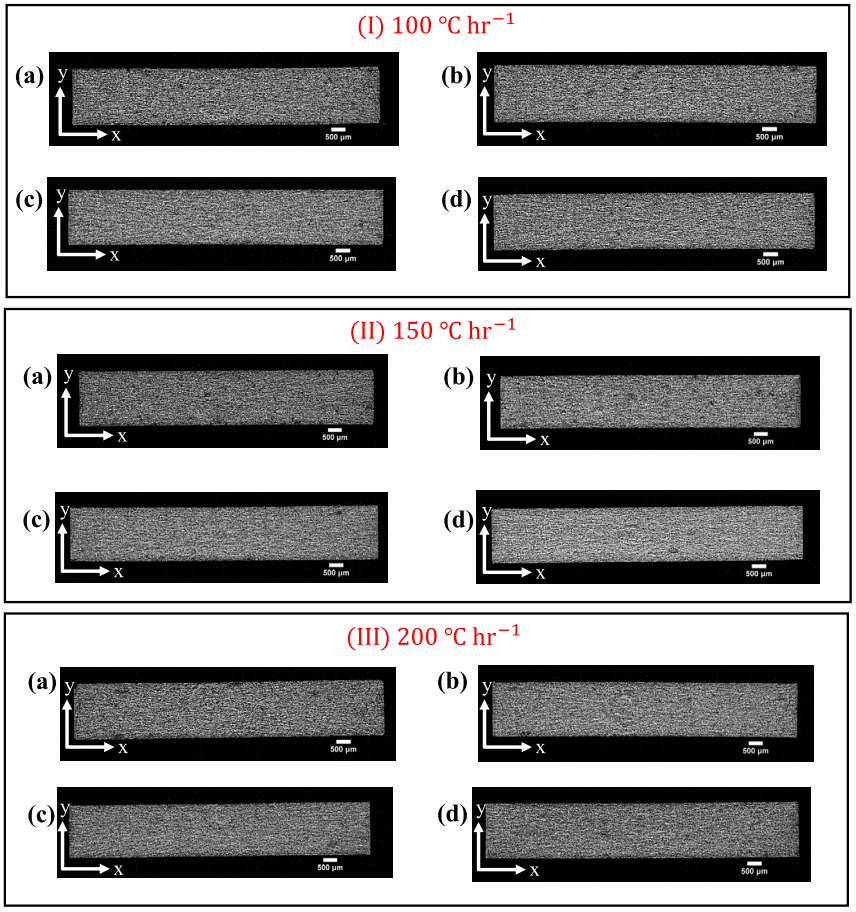

Fig. 6. Reconstructed cross-sectional XμCT images of the alumina samples that were compacted at (a) 7 kN, (b) 23 kN, (c) 40 kN and (d) 58 kN and subsequently fired at 1200 °C at three different heating rates of (I) 100 °C h^{-1}, (II) 150 °C h^{-1} and (III) 200 °C h^{-1}.

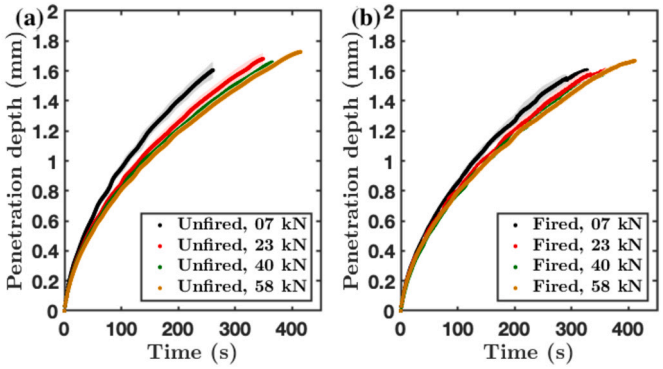

Fig. 7. The liquid penetration depth as a function of time for the 1-octanol transport into the (a) unfired and (b) fired alumina samples at different compaction forces of 7, 23, 40 and 58 kN. The shaded area of each profile corresponds to the standard deviation of each batch.

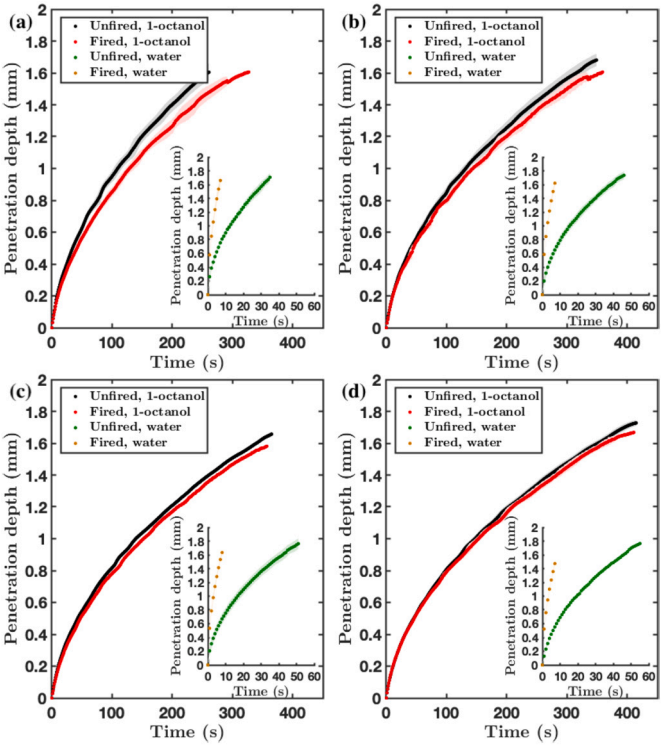

Fig. 8. The liquid penetration profiles of the water and 1-octanol transport into the alumina samples compacted at (a) 7 kN, (b) 23 kN, (c) 40 kN and (d) 58 kN. The fired samples were fired at 1200 °C with a heating rate of 200 °C h^{-1}. The shaded area of each profile corresponds to the standard deviation of each batch. The data of the water transport into the unfired samples and the samples fired at 1200 °C with a heating rate of 200 °C h^{-1} have been reproduced from Al-Sharabi et al. (2021).

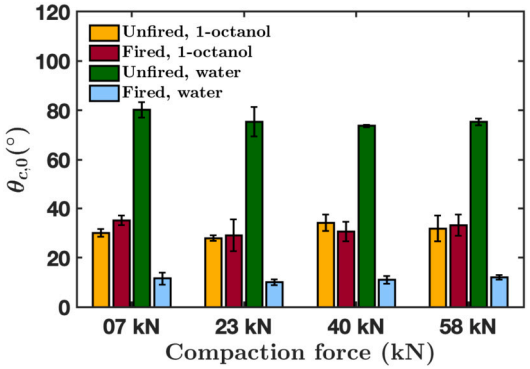

Fig. 9. The initial contact angle of the unfired and fired alumina samples that were compacted at 7, 23, 40 and 58 kN and wetted with 1-octanol and water. The fired samples were fired at 1200 °C with a heating rate of 200 °C h^{-1}. The initial contact angle data of wetting the alumina samples by water have been reproduced from Al-Sharabi et al. (2021).

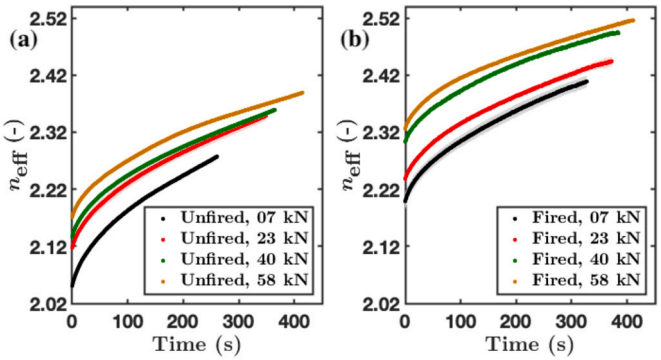

Fig. 10. The change in the refractive index upon the transport of 1-octanol into the (a) unfired and (b) fired samples at the different compaction forces. The fired samples were fired at 1200 °C with a heating rate of 200 °C h^{-1}. The shaded area of each profile corresponds to the standard deviation of each batch.

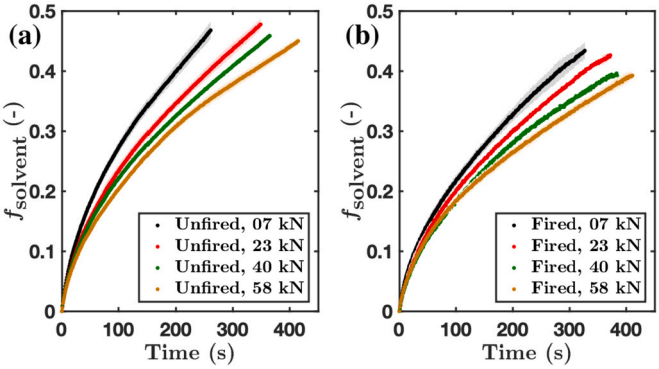

Fig. 11. The change in the fill fraction of 1-octanol into the (a) unfired and (b) fired samples at the different compaction forces. The fired samples were fired at 1200 °C with a heating rate of 200 °C h^{-1}. The shaded area of each profile corresponds to the standard deviation of each batch.

where L is the liquid penetration depth, t is time, γ is the surface tension of liquid, μ is dynamic viscosity of liquid, $R_{h,eq}$ is the hydraulic radius and θ is the contact angle between the solid and liquid.

Since it is possible to observe the position of the reflection peak from the front face of the sample upon the transport of 1-octanol into the sample, the change in the time delay, Δt, can be obtained and then used to determine the change in n_{eff} as a function of time as described in Equation (5).

$$H = \frac{\Delta t c \cos\theta_r}{2n_{eff}} \tag{5}$$

where H is the distance between two interfaces at which reflections of the terahertz radiation occur, c is the speed of light in vacuum and θ_r is the angle of refraction. Since $\cos\theta \approx 1$ for all the unfired and fired samples at the different compaction forces, Equation (5) is simplified as expressed in Equation (6) to obtain the change in n_{eff} as a function of time (Zeitler and Shen, 2012).

$$n_{eff} = \frac{\Delta t c}{2H} \tag{6}$$

Fig. 10 shows the averaged change in n_{eff} of the unfired and fired alumina samples at each compaction force upon the transport of 1-octanol into the sample. n_{eff} of the alumina compact increases with time upon the penetration of 1-octanol in all the unfired and fired samples at the different compaction forces. This is because the penetration of more 1-octanol into the sample matrix increases the concentration of 1-octanol, which has a higher refractive index than air and thus causes an increase in Δt with time.

The information of the change in the effective refractive index of the sample as a function of time, $\Delta n_{eff}(t)$, upon wetting with 1-octanol is of great importance as such information can be used to predict the fill fraction of the solvent in the compact as a function of time, $f_{open,solvent}(t)$, as demonstrated in Equation (7) (Naftaly et al., 2020).

$$f_{open,solvent}(t) = \frac{\Delta n_{eff}(t)}{n_{solvent} - n_{air}} \tag{7}$$

Fig. 11 shows that the fill fraction of 1-octanol in the alumina samples increases as a function of time for each batch. The rate of the solvent filling increases with a decrease in the compaction force within each heat treatment condition, i.e. unfired and fired, as decreasing the compaction force results in an increase in the porosity of the compact.

Further analysis of the negative reflection peak from the sample front face facing the liquid was conducted to investigate the change in the amplitude and width of this peak upon the transport of 1-octanol into the unfired and fired alumina samples at the different compaction forces. This analysis was performed to see if the TPI method can extract any information on whether concentration gradients are getting established during the wetting of the porous alumina samples by 1-octanol. Fig. 12 shows that the peak amplitude decreases as a function of time for both the unfired and fired samples at the different compaction forces of 7, 23, 40 and 58 kN. This is expected as the concentration of 1-octanol increases in the sample and replaces the air in the pores with time (see Fig. A.19 for the absorption spectrum of 1-octanol), which causes more absorption of the terahertz signal and in turn, reduces the amplitude of the reflection peak from the sample front face. It can also be seen that the peak amplitude of the unfired

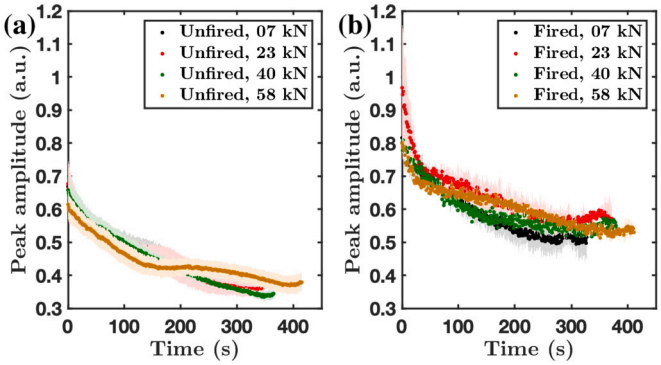

Fig. 12. The change in the amplitude of the reflection peak from the sample front face upon the transport of 1-octanol into the (a) unfired and (b) fired samples at the different compaction forces. The fired samples were fired at 1200 °C with a heating rate of 200 °C h^{-1}. The shaded area of each profile corresponds to the standard deviation of each batch.

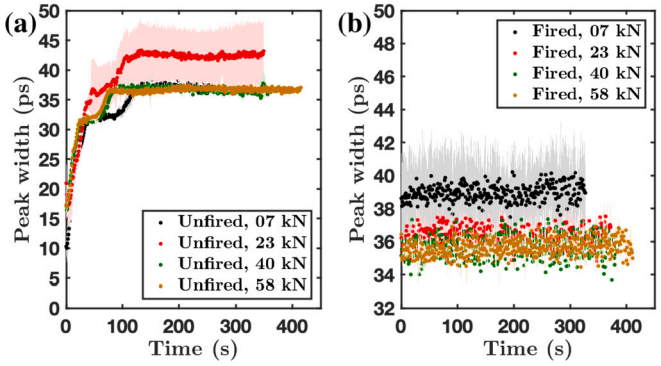

Fig. 13. The change in the width of the reflection peak from the sample front face upon the transport of 1-octanol into the (a) unfired and (b) fired samples at the different compaction forces. The fired samples were fired at 1200 °C with a heating rate of 200 °C h^{-1}. The shaded area of each profile corresponds to the standard deviation of each batch.

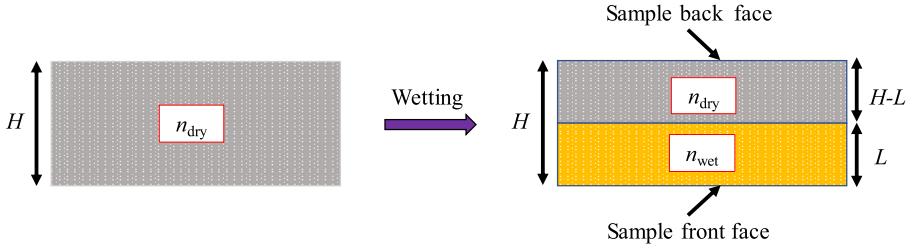

Fig. 14. Schematic of the wetting of a non-swelling alumina sample by 1-octanol. The front face of the sample is exposed to the bulk liquid, whereas the back face of the sample refers to the direction adjacent to the THz optics.

samples is lower compared to the fired samples at the same compaction force. This can be explained by comparing the relative difference between the refractive indices of the two media the terahertz pulse propagates through. The unfired samples have lower refractive index values, as shown in Fig. 2, resulting in a smaller relative difference between the refractive indices and hence a lower peak amplitude is observed for such samples compared to that of the fired samples at the same compaction force.

Fig. 13 shows that the width of the peak from the front face of the unfired samples increases and then becomes constant. This was observed for all the compaction forces of 7, 23, 40 and 58 kN. In contrast, the peak width from the front face of fired samples is constant as a function of time. This might be due to the polymeric additives in the unfired samples, which are removed during the firing process.

The rate of the penetration of 1-octanol into the alumina samples was also quantified using the information obtained from the analysis of the negative reflection peak from the sample front face. For a non-swelling system (Fig. 14), e.g. the alumina sample, the liquid penetration rate was determined by first tracking the amplitude of the reflection peak from the sample front face to determine the change in the time delay, Δt, upon the transport of 1-octanol into the alumina sample, which is then used to calculate the penetration depth, L, as a function of time as expressed in the following equation:

$$L = c\frac{\Delta t - \Delta t_0}{n_{wet} - n_{dry}} \tag{8}$$

The average liquid penetration profiles determined based on the analysis of the reflection peak from the sample front face are shown in Fig. 15. These profiles show that the compaction force and, hence, the alumina sample's porosity impact the penetration of 1-octanol into the alumina samples. The penetration rate of 1-octanol increases with a decrease in the compaction force. The same behaviour is observed for both heat

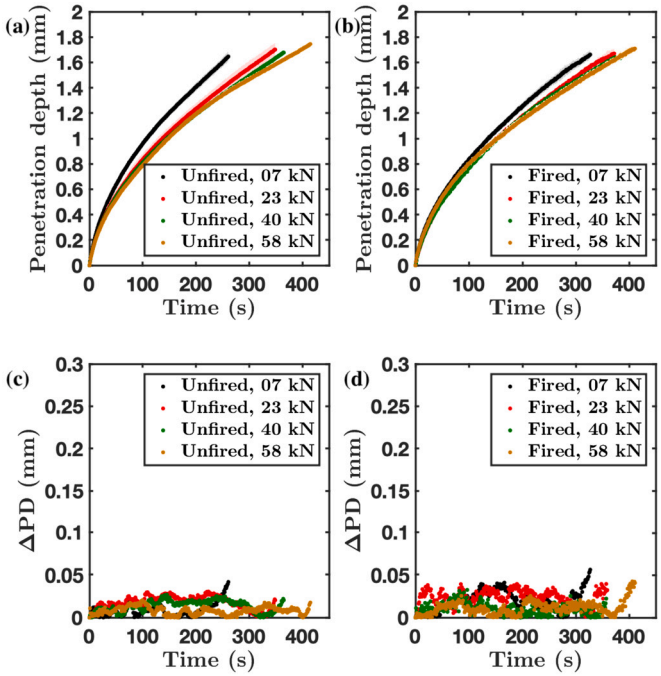

Fig. 15. The liquid penetration depth as a function of time for the 1-octanol transport into the (a) unfired and (b) fired alumina samples at different compaction forces of 7, 23, 40 and 58 kN based on the analysis of the reflection peak from the sample front face. The shaded area of each profile corresponds to the standard deviation of each batch. The difference between the averaged 1-octanol penetration data determined based on the peak of the 1-octanol penetration front and the penetration data determined based on the peak from the sample front face is shown in (c) for the unfired and (d) for the fired samples.

treatment conditions, i.e. fired and fired samples when comparing the 1-octanol transport rates at the different compaction forces within each heat treatment condition. The liquid penetration profiles determined through the analysis of the negative reflection peak from the sample front face are in good agreement with the liquid penetration profiles that were determined by tracking the positive reflection peak from the liquid front (Fig. 7), as indicated by the low residual difference between the penetration rates determined by the two methods for each manufacturing condition (Fig. 15). Analysing the reflection peak from the sample front face sheds light on additional helpful information that can be extracted using the TPI method.

3.4. Liquid transport kinetics

A simple power law, defined in Equation (9) (Yassin et al., 2015a; Markl and Zeitler, 2017; Markl et al., 2018; Al-Sharabi et al., 2021), was fitted to the time-resolved data of the liquid penetration rates to extract the values of parameters k and m.

$$y(t) = kt^m \tag{9}$$

where k is a fitting parameter that describes the transport rate of the liquid into the sample and the exponent m describes the type of the mass transport mechanism (Al-Sharabi et al., 2021). An m value of 0.5 indicates that the transport process obeys Darcy flow, which is driven by a capillary pressure gradient, whereas a value of m between 0.5 and 1 suggests anomalous transport (Markl and Zeitler, 2017; Al-Sharabi et al., 2020).

It can be seen from Fig. 16 that the parameter k acquired from fitting the water transport data with the power law increases with an increase in the porosity of the sample within each heating treatment condition, indicating that the water transports faster at higher porosity, i.e. lower compaction force. This is consistent with the findings of the TPI water transport measurements on other ceramic powder compacts, such as functionalised calcium carbonate (FCC) (Markl et al., 2018) and di-calcium phosphate (DCP) (Skelbæk-Pedersen et al., 2020) where a linear relationship between the parameter k and porosity was observed. In addition, the parameter k for the alumina samples fired at a heating rate of 200 °C h^{-1} has the highest values compared to the other heating rates of 100 and 150 °C h^{-1} at the same compaction force. However, Fig. 16 shows that the parameter k obtained from fitting the 1-octanol transport data with the power law increases as the porosity increases within each heat treatment condition, i.e. unfired and fired. The parameter k measured for the 1-octanol transport has smaller values than the values of the water transport data at the same manufacturing conditions, indicating the slower transport of 1-octanol into the alumina sample. The k values of the water penetration into the alumina samples fired at 1200 °C with a heating rate of 200 °C h^{-1} are 9 - 10 times higher than the values of 1-octanol at the same compaction force, i.e. same porosity. The dynamic viscosity of water is 9 times smaller than that of 1-octanol, which shows the correlation between the k parameter and dynamic viscosity, i.e. a change in the dynamic viscosity causes a change in the k parameter at a similar magnitude for the alumina samples that were prepared at the same compaction and firing conditions. The values of the parameter m suggest that the transport of water and 1-octanol can be considered Darcy flow dominated by a gradient in the capillary pressure across the alumina compact.

The terahertz liquid transport results revealed the effect of the polarity of the solvent on the transport kinetics in the unfired samples containing polymeric additives and the fired samples without the additives at the different compaction forces. Such results show the potential of the TPI method to provide a better understanding of the interaction between the different solvents and the porous ceramic catalysts during the manufacturing processes and the heterogeneous catalysis. The terahertz transport measurements complement the information that can be captured with other techniques, such as PFG NMR and neutron diffraction (Mantle et al., 2010; D'Agostino et al., 2012; McGregor et al., 2015), to provide a further understanding of the liquid transport characteristics of porous ceramic powder compacts. It is important to note that the terahertz transport measurements also complement the terahertz-time-domain spectroscopy measurements of the relaxation dynamics of molecular dipoles in solution,

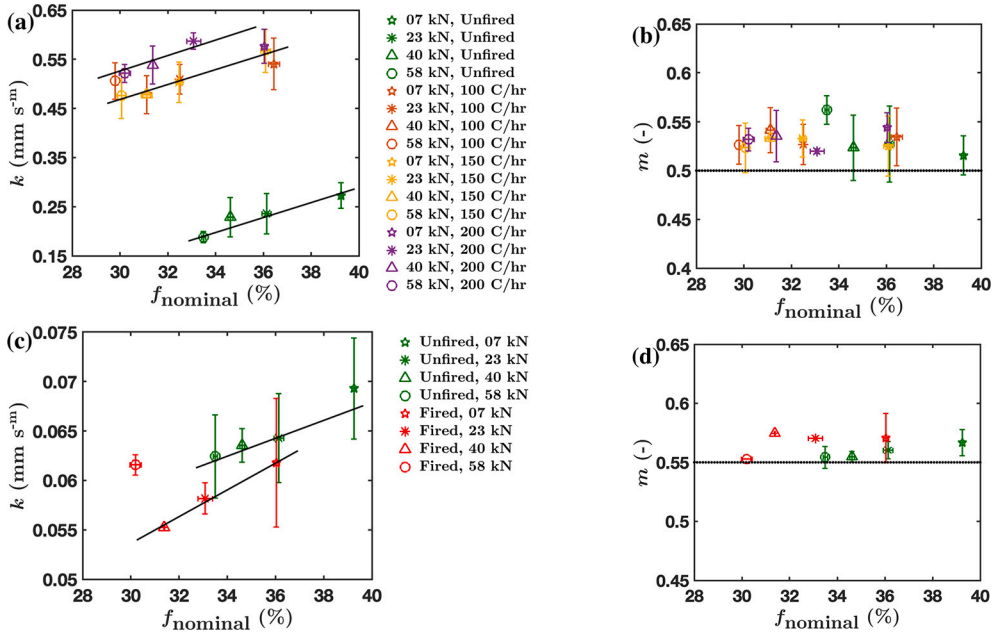

Fig. 16. Characteristic parameters extracted from the liquid penetration profiles using the power law (Equation (9)). (a and b) The parameters k and m obtained from the power law fitting of the rates of water penetration into the alumina samples: compacted at 7, 23, 40 and 58 kN; unfired and fired at 1200 °C with heating rates of 100, 150 and 200 °C h^{-1}. (c and d) The parameters k and m obtained from the power law fitting of the rates of 1-octanol penetration into the alumina samples: compacted at 7, 23, 40 and 58 kN; unfired and fired at 1200 °C with a heating rate of 200 °C h^{-1}. The black lines are added to guide the eye. The data of the water transport into the unfired samples and the samples fired at 1200 °C with a heating rate of 200 °C h^{-1} have been reproduced from Al-Sharabi et al. (2021).

as reported by McGregor et al. (2015). Gaining a better understanding of the transport of different solvents in a range of catalyst compacts will help scientists in the catalyst field design catalysts with the desired quality and properties.

4. Conclusions

The TPI method was successfully applied to understand the impact of the sintering conditions, i.e. heating rate in this work, on the water ingress into a range of alumina powder compacts. The samples fired at a heating rate of 200 °C h^{-1} has the fastest rate of water ingress in comparison with the samples fired at the other heating rates of 100 and 150 °C h^{-1} at the same compaction force. A better understanding of the effect of the different sintering parameters involved in the sintering process on the liquid transport kinetics is crucial for optimising the synthesis of catalytic materials, saving energy and hence reducing the operational costs of catalyst manufacturing as well as achieving the desired liquid transport kinetics. The TPI technique was also established for quantifying the transport kinetics of less polar solvents, 1-octanol, in this study and showed how the type of solvent significantly impacts the liquid transport kinetics in the alumina powder compacts. The transparency of the less polar solvents to terahertz radiation shows that valuable information can be obtained using the TPI method, such as the change in the n_{eff} of the ceramic powder compact upon the transport of the less polar solvent which can then be used to calculate the fill fraction of the solvent in the compact. Investigating different solvents is vital to better understand the interaction of the different solvents during both the manufacturing and the liquid-phase reactions over heterogeneous solid catalysts. The TPI results demonstrated in this work shed light on developing ceramic catalysts and catalyst supports by providing quantitative analysis of the impact of the heating rate and the type of solvent on the liquid transport kinetics in such materials.

Declaration of competing interest

The authors declare the following financial interests/personal relationships which may be considered as potential competing interests: Mohammed Al-Sharabi reports financial support was provided by Johnson Matthey Plc. Mohammed Al-Sharabi reports financial support was provided by Engineering and Physical Sciences Research Council.

Data availability

Data will be made available on request.

Acknowledgements

We would like to thank Johnson Matthey and the U.K. Engineering and Physical Sciences Research Council (EPSRC) for their funding through an iCASE award (1943009). We would also like to thank Marian Bentley, Michele Marigo and Karen Huang for their feedback and help preparing the alumina powder compacts. For the purpose of open access, the authors have applied a Creative Commons Attribution (CC BY) licence to any Author Accepted Manuscript version arising from this submission.

Appendix A. Supporting information

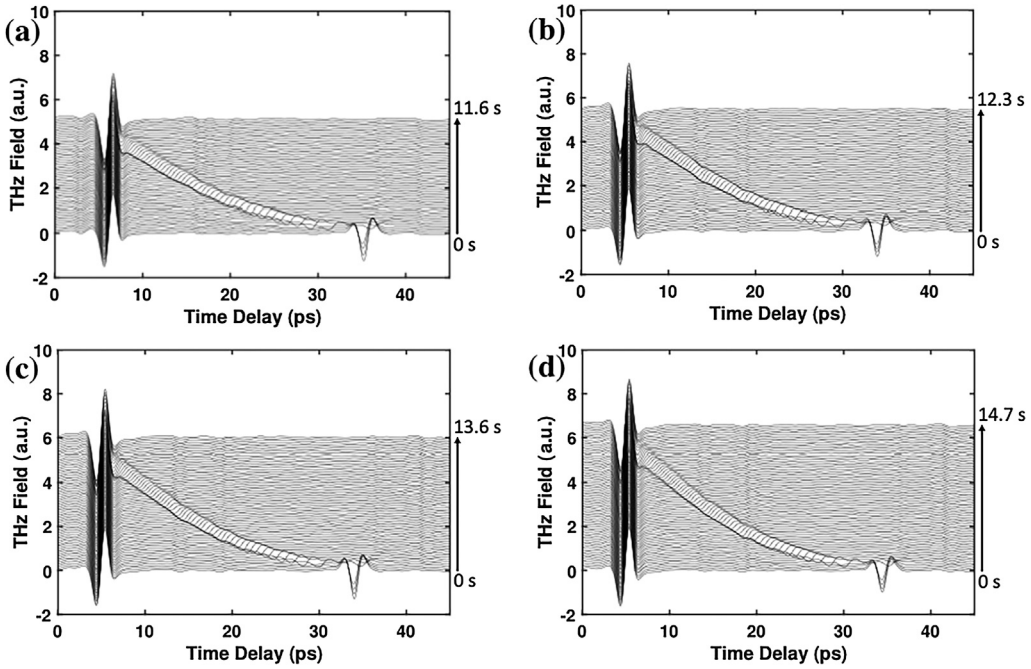

Fig. A.17. The deconvolved terahertz waveforms presented in stacked plots (waterfall plots) to show the water penetration into a set of alumina samples that were compacted at (a) 7 kN, (b) 23 kN, (c) 40 kN and (d) 58 kN and subsequently fired at 1200 °C with a heating rate of 150 °C h^{-1}. Each third deconvolved waveform was plotted with an offset of 0.03 a.u. between each deconvolved waveform to enable the visualisation of the water front movement into the sample. The total duration (in seconds) of the full penetration of water into the sample is represented by the arrow on the right each plot.

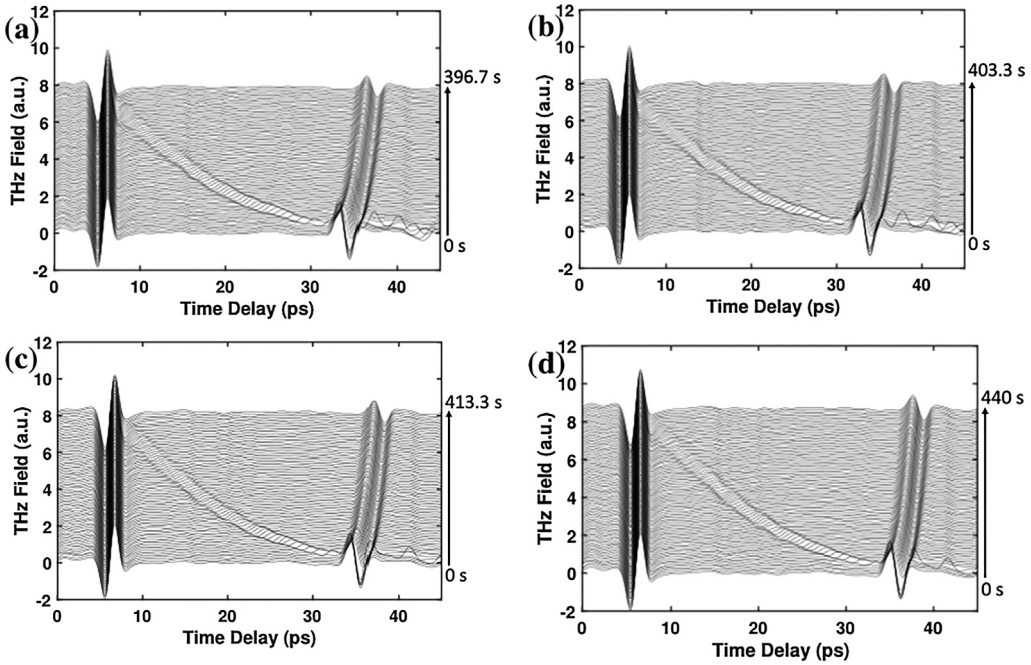

Fig. A.18. The deconvolved terahertz waveforms presented in stacked plots to show the 1-octanol penetration into a set of alumina samples that were compacted at (a) 7 kN, (b) 23 kN, (c) 40 kN and (d) 58 kN and subsequently fired at 1200 °C with a heating rate of 200 °C h^{-1}. Each fifth deconvolved waveform was plotted with an offset of 0.02 a.u. between each deconvolved waveform to enable the visualisation of the 1-octanol front movement into the sample. The total duration (in seconds) of the full penetration of 1-octanol into the sample is represented by the arrow on the right each plot.

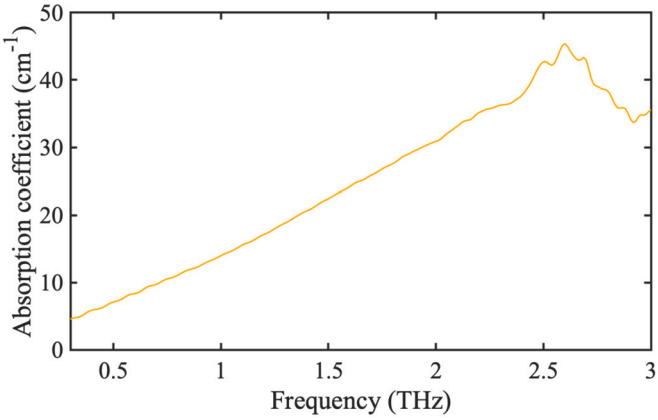

Fig. A.19. The absorption coefficient of 1-octanol as a function of frequency.

References

Al-Sharabi, M., Markl, D., Mudley, T., Bawuah, P., Karttunen, A.-P., Ridgway, C., Gane, P., Ketolainen, J., Peiponen, K.-E., Rades, T., Zeitler, J.A., 2020. Simultaneous investigation of the liquid transport and swelling performance during tablet disintegration. Int. J. Pharm. 584, 119380.

Al-Sharabi, M., Markl, D., Vivacqua, V., Bawuah, P., MacLean, N., Bentley, M., York, A.P.E., Marigo, M., Huang, K., Zeitler, J.A., 2021. Terahertz pulsed imaging as a new method for investigating the liquid transport kinetics of α-alumina powder compacts. Chem. Eng. Res. Des. 165, 386–397.

Amaya, D.M., Estrada, D., Hotza, D., Rodrigues Neto, J.B., Escobar, J.A., 2017. Porous Cu/YSZ anodes processed by aqueous tape casting for IT-SOFC. J. Eur. Ceram. Soc. 37, 5233–5237.

Bawuah, P., Markl, D., Farrell, D., Evans, M., Portieri, A., Anderson, A., Goodwin, D., Lucas, R., Zeitler, J.A., 2020. Terahertz-based porosity measurement of pharmaceutical tablets: a tutorial. J. Infrared Millim. Terahertz Waves 41, 450–469.

Boccaccini, A.R., Trusty, P.A., 1998. In situ characterization of the shrinkage behavior of ceramic powder compacts during sintering by using heating microscopy. Mater. Charact. 41, 109–121.

Cai, J., Jin, T., Kou, J., Zou, S., Xiao, J., Meng, Q., 2021. Lucas–Washburn equation-based modeling of capillary-driven flow in porous systems. Langmuir 37, 1623–1636.

Chen, P., Kim, G.-Y., Ni, J., 2007. Investigations in the compaction and sintering of large ceramic parts. J. Mater. Process. Technol. 190, 243–250.

Choi, J.-S., Lee, S.W., Kim, Y.H., 2020. Low-temperature synthesis of α-alumina using NaCl–Na3AlF6 flux. Ceram. Int. 46, 13233–13239.

D'Agostino, C., Mitchell, J., Gladden, L.F., Mantle, M.D., 2012. Hydrogen bonding network disruption in mesoporous catalyst supports probed by PFG-NMR diffusometry and NMR relaxometry. J. Phys. Chem. C 116, 8975–8982.

Das, P.K., Li, X., Liu, Z.-S., 2010. Analysis of liquid water transport in cathode catalyst layer of PEM fuel cells. Int. J. Hydrog. Energy 35, 2403–2416.

Dong, R., DiNunzio, J.C., Regler, B.P., Wasylaschuk, W., Socia, A., Zeitler, J.A., 2021. Insights into the control of drug release from complex immediate release formulations. Pharmaceutics 13, 933.

Dong, R., Nassar, M., Friend, B., Teckoe, J., Zeitler, J.A., 2023. Studying the dissolution of immediate release film coating using terahertz pulsed imaging. Int. J. Pharm. 630, 122456.

Dong, R., Zeitler, J.A., 2022. Visualising liquid transport through coated pharmaceutical tablets using terahertz pulsed imaging. Int. J. Pharm. 619, 121703.

Faure, R., Rossignol, F., Chartier, T., Bonhomme, C., Maître, A., Etchegoyen, G., Del Gallo, P., Gary, D., 2011. Alumina foam catalyst supports for industrial steam reforming processes. J. Eur. Ceram. Soc. 31, 303–312.

Hammel, E.C., Ighodaro, O.L.-R., Okoli, O.I., 2014. Processing and properties of advanced porous ceramics: an application based review. Ceram. Int. 40, 15351–15370.

Jaine, J.E., Mucalo, M.R., 2015. Measurements of the wettability of catalyst support materials using the Washburn capillary rise technique. Powder Technol. 276, 123–128.

Jonuscheit, J., 2018. Terahertz techniques in NDE. In: Handbook of Advanced Non-Destructive Evaluation. Springer, Cham, Cham, pp. 1–20.

Kempen, D., Piccolroaz, A., Bigoni, D., 2019. Thermomechanical modelling of ceramic pressing and subsequent sintering. Int. J. Mech. Sci. 156, 146–158.

Kim, B.-N., Morita, K., Suzuki, T.S., Li, J.-G., Matsubara, H., 2021. Simulation of densification behavior of nano-powder in final sintering stage: effect of pore-size distribution. J. Eur. Ceram. Soc. 41, 625–634.

Kumar, A., Mohanta, K., Kumar, D., Parkash, O., 2014. Green properties of dry-pressed alumina compacts fabricated using sucrose as binder. Ceram. Int. 40, 6271–6277.

Lapuerta, M., Rodríguez-Fernández, J., Patiño-Camino, R., Cova-Bonillo, A., Monedero, E., Meziani, Y.M., 2020. Determination of optical and dielectric properties of blends of alcohol with diesel and biodiesel fuels from terahertz spectroscopy. Fuel 274, 117877.

Lewis, R., 2017. Materials for terahertz engineering. In: Kasap, S., Capper, P. (Eds.), Springer Handbook of Electronic and Photonic Materials. Springer, Cham, Switzerland, pp. 1339–1350.

Luo, Y., Wang, X., Wang, C., Hu, Y., Liu, M., 2018. Alpha-to-gamma reverse phase transformation of molten removal in alumina ceramics laser processing. Ceram. Int. 44, 10412–10419.

Lysova, A.A., Bergwerff, J.A., Espinosa-Alonso, L., Weckhuysen, B.M., Koptyug, I.V., 2010. Magnetic resonance imaging as an emerging tool for studying the preparation of supported catalysts. Appl. Catal. A, Gen. 374, 126–136.

Lysova, A.A., Koptyug, I.V., Sagdeev, R.Z., Parmon, V.N., Bergwerff, J.A., Weckhuysen, B.M., 2005. Noninvasive in situ visualization of supported catalyst preparations using multinuclear magnetic resonance imaging. J. Am. Chem. Soc. 127, 11916–11917.

Mantle, M.D., Enache, D.I., Nowicka, E., Davies, S.P., Edwards, J.K., D'Agostino, C., Mascarenhas, D.P., Durham, L., Sankar, M., Knight, D.W., Gladden, L.F., Taylor, S.H., Hutchings, G.J., 2010. Pulsed-field gradient NMR spectroscopic studies of alcohols in supported gold catalysts†. J. Phys. Chem. C 115, 1073–1079.

Markl, D., Wang, P., Ridgway, C., Karttunen, A.-P., Bawuah, P., Ketolainen, J., Gane, P., Peiponen, K.-E., Zeitler, J.A., 2018. Resolving the rapid water absorption of porous functionalised calcium carbonate powder compacts by terahertz pulsed imaging. Chem. Eng. Res. Des. 132, 1082–1090.

Markl, D., Yassin, S., Wilson, D.I., Goodwin, D.J., Anderson, A., Zeitler, J.A., 2017. Mathematical modelling of liquid transport in swelling pharmaceutical immediate release tablets. Int. J. Pharm. 526, 1–10.

Markl, D., Zeitler, J.A., 2017. A review of disintegration mechanisms and measurement techniques. Pharm. Res. 34, 890–917.

McGregor, J., Li, R., Zeitler, J.A., D'Agostino, C., Collins, J.H.P., Mantle, M.D., Manyar, H., Holbrey, J.D., Falkowska, M., Youngs, T.G.A., Hardacre, C., Stitt, E.H., Gladden, L.F., 2015. Structure and dynamics of aqueous 2-propanol: a THz-TDS, NMR and neutron diffraction study. Phys. Chem. Chem. Phys. 17, 30481–30491.

Montilha, F.S., Rocco, F.O., Melo, C.C., Sciuti, V.F., Canto, R.B., 2018. Identification of dilatancy in green compacted ceramic powder via digital image correlation. Powder Technol. 330, 471–476.

Munnik, P., de Jongh, P.E., de Jong, K.P., 2015. Recent developments in the synthesis of supported catalysts. Chem. Rev. 115, 6687–6718.

Munro, M., 1997. Evaluated material properties for a sintered alpha-alumina. J. Am. Ceram. Soc. 80, 1919–1928.

Naftaly, M., Tikhomirov, I., Hou, P., Markl, D., 2020. Measuring open porosity of porous materials using THz-TDS and an index-matching medium. Sensors 20, 1–11.

Nagasawa, H., Omura, T., Asai, T., Kanezashi, M., Tsuru, T., 2020. Filtration of surfactant-stabilized oil-in-water emulsions with porous ceramic membranes: effects of membrane pore size and surface charge on fouling behavior. J. Membr. Sci. 610, 118210.

Nijhuis, T.A., Beers, A.E.W., Vergunst, T., Hoek, I., Kapteijn, F., Moulijn, J.A., 2001. Preparation of monolithic catalysts. Catal. Rev. 43, 345–380.

Obradovic, J., Collins, J.H.P., Hirsch, O., Mantle, M.D., Johns, M.L., Gladden, L.F., 2007. The use of THz time-domain reflection measurements to investigate solvent diffusion in polymers. Polymer 48, 3494–3503.

Okuma, G., Gonzalez-Julian, J., Guillon, O., Wakai, F., 2018. Comparison between sinter forging and X-ray microtomography methods for determining sintering stress and bulk viscosity. J. Eur. Ceram. Soc. 38, 2053–2058.

Pechenkin, A.A., Badmaev, S.D., Belyaev, V.D., Sobyanin, V.A., 2015. Performance of bifunctional SuO–CeO2/γ-Al2O3 catalyst in dimethoxymethane steam reforming to hydrogen-rich gas for fuel cell feeding. Appl. Catal. B, Environ. 166–167, 535–543.

Pickwell, E., Wallace, V.P., 2006. Biomedical applications of terahertz technology. J. Phys. D, Appl. Phys. 39, R301–R310.

Rytter, E., Borg, Ø., Enger, B.C., Holmen, A., 2019. α-alumina as catalyst support in Co Fischer-Tropsch synthesis and the effect of added water; encompassing transient effects. J. Catal. 373, 13–24.

Sievers, C., Noda, Y., Qi, L., Albuquerque, E.M., Rioux, R.M., Scott, S.L., 2016. Phenomena affecting catalytic reactions at solid–liquid interfaces. ACS Catal. 6, 8286–8307.

Skelbæk-Pedersen, A.L., Al-Sharabi, M., Vilhelmsen, T.K., Rantanen, J., Zeitler, J.A., 2020. Effect of particle size and deformation behaviour on water ingress into tablets. Int. J. Pharm. 587, 119645.

Soundaranathan, M., Al-Sharabi, M., Sweijen, T., Bawuah , P., Zeitler, J.A., Hassanizadeh, S.M., Pitt, K., Johnston, B.F., Markl, D., 2023. Modelling the evolution of pore structure during the disintegration of pharmaceutical tablets. Pharmaceutics 15.

Trenzado, J.L., Matos, J.S., Alcalde, R., 2003. Volumetric properties and viscosities of the methyl butanoate + heptane + 1-octanol ternary system and its binary constituents in the temperature range from 283.15 to 313.15 K. Fluid Phase Equilib. 205, 171–192.

Wan, L., Guo, X., Li, K., Yan, J., 2020. Preparation of porous SiC-Al2O3 ceramics with spherical shell structures of large surface area and high strength. Ceram. Int. 46, 10325–10331.

Werner, J., Besser, B., Brandes, C., Kroll, S., Rezwan, K., 2014. Production of ceramic membranes with different pore sizes for virus retention. J. Water Process Eng. 4, 201–211.

Wu, Z., Hu, W., Luo, Y., Sun, L., Wang, J., 2018. Porous γ-(Y1-xHox)2Si2O7 thermal insulator with excellent high-temperature strength retention and very low thermal conductivity. J. Eur. Ceram. Soc. 38, 3347–3353.

Xu, J., Plaxco, K.W., Allen, S.J., 2006. Absorption spectra of liquid water and aqueous buffers between 0.3 and 3.72 THz. J. Chem. Phys. 124, 036101.

Yang, R., Qi, Z., Gao, Y., Yang, J., Zhou, Y., Liu, H., Peng, L., Jiao, J., 2020. Effects of alumina sols on the sintering of α-alumina ceramics. Ceram. Int.

Yassin, S., Goodwin, D.J., Anderson, A., Sibik, J., Wilson, D.I., Gladden, L.F., Zeitler, J.A., 2015a. The Disintegration process in microcrystalline cellulose based tablets, part 1: influence of temperature, porosity and superdisintegrants. J. Pharm. Sci. 104, 3440–3450.

Yassin, S., Su, K., Lin, H., Gladden, L.F., Zeitler, J.A., 2015b. Diffusion and swelling measurements in pharmaceutical powder compacts using terahertz pulsed imaging. J. Pharm. Sci. 104, 1658–1667.

Zeitler, J.A., Shen, Y.-C., 2012. Industrial applications of terahertz imaging. In: Peiponen, K.-E., Zeitler, J.A., Kuwata-Gonokami, M. (Eds.), Terahertz Spectroscopy and Imaging. In: Springer Series in Optical Sciences. Springer, Berlin, Heidelberg, pp. 451–489.

Zhokh, A.A., Strizhak, P.E., 2017. Effect of zeolite ZSM-5 content on the methanol transport in the ZSM-5/alumina catalysts for methanol-to-olefin reaction. Chem. Eng. Res. Des. 127, 35–44.